JOURNAL OF SOLID STATE CHEMISTRY **139,** 66–78 (1998)
ARTICLE NO. SC987808

Structure, Cation Distribution, and Properties of Nanocrystalline Titanomagnetites Obtained by Mechanosynthesis: Comparison with Soft Chemistry

N. Millot,* S. Begin-Colin,† P. Perriat,* and G. Le Caër†

*Laboratoire de Recherches sur la Réactivité des Solides, U.M.R. 5613, B.P. 400, 21011 Dijon Cedex, France; and
†Laboratoire de Science et Génie des Matériaux Métalliques, U.M.R. 7584, 54042 Nancy Cedex, France

Received October 27, 1997; in revised form February 23, 1998; accepted February 24, 1998

Nanocrystalline Fe-based spinels with composition $Fe_{2.5}Ti_{0.5}O_4$ were synthesized using two different routes: soft chemistry and high-energy ball milling. In the first case, two steps were involved: precipitation in an aqueous solution followed by thermal annealing under a reducing mixture of $N_2/H_2/H_2O$ gases. In the second case, the spinel phase was directly formed in the mill at room temperature and under argon atmosphere from Fe, Fe_2O_3, and TiO_2 in stoichiometric proportions. The as-prepared powders are characterized by X-ray diffraction, scanning and transmission electron microscopy, surface area measurement, and Mössbauer spectrometry. In both cases, the crystallite's size is about 15 nm, but whereas in the case of mechanosynthesis, the ball-milled powders consist of aggregates, those obtained by soft chemistry are very well dispersed. In contrast to the soft chemistry route, both lattice defects and cation site inversion are induced by high energy ball milling, as evidenced by X-ray diffraction and thermogravimetric analysis. Finally, the particle coercivity is studied and discussed according to particle size and the degree of oxidation of Fe cations inferred from thermogravimetry. © 1998 Academic Press

Key Words: **Titanium ferrite; mechanosynthesis; soft chemistry; nanometric particles; spinels; X-ray diffraction; Mössbauer spectrometry.**

1. INTRODUCTION

The magnetic properties of powders of various iron-based spinels $Fe_{3-x}M_xO_4$, where $0 \leq x \leq 1$ and M is a cation such as Mn, Zn, Cr, Mo, V, Cu, or Ti (1–2), have been thoroughly studied over many decades. A change of the cation-to-anion ratio in the spinel phase leading to a deviation δ from stoichiometry, $(Fe_{3-x}M_x)_{1-\delta}O_4$ is possible. When the compound contains only Fe cations, δ is directly related to the fraction of Fe^{2+} which is oxidized into Fe^{3+}. It can be positive or negative according to the nature of the defects: cationic vacancies ($\delta > 0$) or cation interstitials ($\delta < 0$). When the compound also contains some M cations whose degree of oxidation can change, δ is further related to its valence. In principle, δ could be varied in the spinel phase from negative values to a maximum one corresponding to the highest valence of each cation ($\delta_{max} = 1/9$ for $Fe_{3-3\delta}O_4$). However, the full range of δ has very rarely been investigated for the spinel phase with a given grain size, so that properties as simple as the thermodynamic relationship between δ and pO_2 at a given temperature have never been determined experimentally. For very small grain size (≤ 10 nm), low temperatures are required to stabilize nanometer-sized grains. Unfortunately, in room conditions and even in less restricted conditions (temperature lower than 500°C and pO_2 higher than 10^{-5} Pa), the Fe^{2+} cations are not thermodynamically stable and are almost completely oxidized to Fe^{3+}, so that compounds with $\delta \sim 0$ cannot be investigated. In contrast, δ cannot be increased significantly without precipitation of some other phases in spinels with grain sizes larger than 100 nm, which are generally synthesized at high temperatures. A phase transition depending on grain size was indeed found by Multani (3) in the case of γ-Fe_2O_3 (γ-Fe_2O_3 below a critical size of about 30 nm, α-Fe_2O_3 above). Dieckmann also showed that some phase transition is observed for very small δ in Fe-based spinels with micrometer-sized grains annealed at high temperature (4).

The present work is part of a general study of the evolution of the physical and thermodynamical properties of some substituted magnetites with a spinel structure at a given grain size as a function of δ. Toward that aim, chemical composition and synthesis methods have been selected as described in the following section.

2. SELECTION OF SPINEL COMPOSITION AND SYNTHESIS METHODS

An intermediate grain size range (10–50 nm) has been chosen, as $M = Fe$, γ-Fe_2O_3 powders ($\delta = \delta_{max}$) have

0022-4596/98 $25.00

mainly been studied for grain sizes lower than 10 nm, while Fe_3O_4 powders ($\delta \approx 0$) have been characterized for grain sizes larger than 50 nm. Moreover, some $M \neq Fe$ cations must be introduced into magnetite both to stabilize the spinel structure for high δ and to avoid grain growth. We have thus selected $M = Ti$, which fulfills the required conditions. The Ti content has been determined from two arguments. First, a content close to that of natural titanomagnetites, $Fe_{2.4}Ti_{0.6}O_4$ (5) has been chosen. Contrary to what was believed in the seventies (6–11), rocks contain not only micrometric inclusions but also nanometric clusters of titanomagnetites (10). Further magnetic studies of these compounds, very rarely found in the literature, may thus provide new information to scientists who investigate the history of Earth. Second, the selected titanomagnetite must be easily synthesized by soft chemistry; as previous trials with oxalate precursors have shown that the synthesis of titanomagnetites $Fe_{3-x}Ti_xO_4$ with $x \geq 0.5$ is difficult and has been performed only once (12, 13), a Ti content $x = 0.5$ has finally been selected.

In the spinel structure, two types of sites can be occupied by the cations (14): tetrahedral (A) or octahedral (B). When the ferrite contains some M cations, the cation distribution is not as simple as it is in magnetite, where all the Fe^{2+} ions are on B sites. In the case of titanium ferrite, the distribution of cations has been extensively studied using several methods. All the authors have found the Ti^{4+} cations residing on octahedral sites but the location of the Fe^{2+} cations is still controversial even when studied by the same technique. In the fifties, two extreme models were suggested. Based on magnetic measurements, Akimoto proposed that all the additional Fe^{2+} cations are on A sites (15),

$$[Fe_x^{2+}Fe_{1-x}^{3+}]_A[Fe^{2+}Fe_{1-x}^{3+}Ti_x^{4+}]_BO_4, \qquad [1]$$

while, according to Néel (16) and Chevalier (17), the distribution of the cations, which depends on x, exhibits the crystal-chemical preference of Fe^{2+} for the B sublattice and Fe^{3+} for the A one:

$$[Fe^{3+}]_A[Fe_{1+x}^{2+}Fe_{1-2x}^{3+}Ti_x^{4+}]_BO_4 \quad \text{for } x \leq 0.5$$

$$[Fe_{2-2x}^{3+}Fe_{2x-1}^{2+}]_A[Fe_{2-x}^{2+}Ti_x^{4+}]_BO_4 \quad \text{for } x > 0.5. \qquad [2]$$

Since these two extreme suggestions, more sophisticated distributions have been proposed. An intermediate model, following that of Akimoto in the range $0.2 \leq x \leq 0.8$ but that of Néel and Chevalier otherwise, has been proposed by O'Reilly (18). Moreover, the cation distribution has been shown to be temperature-dependent from thermoelectric coefficient measurements by Trestman-Matts (19) in accordance with predictions by O'Neill and Navrotsky (20). In any case the dispute may originate from differences in several experimental conditions and control parameters, such as temperature, grain size, deviation from stoichiometry, and method of synthesis.

In this context two routes, soft chemistry and mechanosynthesis, which lead to powder particles with nanometer-sized grains of a given mean size but lead a priori to very different states of powder aggregation, defect contents, and probably also chemical-crystal preference of the cations, have been selected.

Among the numerous methods of soft chemistry, a precipitation which yields a large quantity of powder (about 10 g) with nanometer-sized grains has been chosen (21, 22). The as-prepared compounds are most often studied without further thermal annealing. In the present paper, the precipitation step was followed by varying treatments to eliminate remaining impurities and to reach a stoichiometric state ($\delta \approx 0$). The annealing conditions were optimized to avoid any significant grain growth up to 500°C. For these temperatures, oxygen partial pressures, pO_2, of about 10^{-20}–10^{-25} Pa were applied to obtain very small deviations from stoichiometry. These partial oxygen pressures are established from $N_2/H_2/H_2O$ gas mixtures controlled using a specific device previously described (23).

The second synthesis route is mechanosynthesis (24–26). In this framework, three methods for obtaining nanometric ferrites have been described in the literature:

— grinding of micrometric materials (comminution) easily prepared by classical solid state reactions,

— mechanical activation, which consists of milling some starting precursors and then annealing ground powders at low temperatures to avoid grain growth, and

— mechanochemical synthesis from a mixture of compounds in stoichiometric proportions.

A redistribution of the M cations between the two sublattices has been observed to take place during grindings of Zn (27–29), Mg (28), Ni (28), and Ni–Zn ferrite (30). The formation of Zn ferrite starting from mechanically activated mixtures of Fe_2O_3 and ZnO by annealing at 800°C has been reported (31). Finally, the direct mechanosynthesis of ferrites, such as Si (32), Ni (33), and Co (34) ferrites, has been investigated. Except in the case of the Ni ferrite, a single pure phase has never been obtained. Nanomagnetite has also been prepared by dry-grinding of hematite under vacuum or argon atmosphere (35) or wet-milling of hematite in water (36). Magnetite may also be obtained by grinding a mixture of α-Fe_2O_3 and Fe (37–40). In all cases the duration of mechanosynthesis is very long and may lead to large Cr and Ni contamination (about 9 at%). In the present work, we seek conditions for direct synthesis to obtain a pure single phase without significant contamination. Moreover, the synthesis of titanomagnetites is more complicated than the mechanosynthesis of ferrites reported in the literature. When the substituting cation is Ti^{4+}, δ may indeed vary due to the oxidation of some Fe^{2+}. The mechanosynthesis of titanomagnetites with well-controlled

$\delta \neq \delta_{max}$ then requires an inert atmosphere to minimize eventual oxidation of ground powders.

In this paper, we focus mainly on the formation of $Fe_{2.5}Ti_{0.5}O_4$ by mechanosynthesis, studying the influence of the duration and the energetical conditions of milling on the purity of the spinel phase and the grain size. The properties of as-milled ferrites are compared to those of ferrites prepared by soft chemistry.

3. EXPERIMENTAL

3.1. Powder Synthesis

The soft chemistry in this experiment processes are:

(1) Suitable amounts of ferrous, ferric, and titanium chloride are dissolved in HCl solution. Cation concentrations (≈ 0.3 mol.l^{-1}) and pH (< 1) are low enough to prevent any titanium or iron oxide and hydroxide precipitation.

(2) The above solution is added into an ammonia solution. The system was continuously stirred at 800 rpm. The precipitation is instantaneous. Precipitate is separated by centrifugation. The equation of the reaction is

$$3/2\ Fe^{2+} + Fe^{3+} + 1/2\ Ti^{4+} + 8\ OH^- \rightarrow Fe_{2.5}Ti_{0.5}O_4 + 4\ H_2O. \quad [3]$$

(3) The solution is washed with deionized water under ultrasonication for 5 min. and then separation by centrifugation at 3,500 rpm for 5 min. After four washings centrifugation is no longer possible; a sol is formed.

(4) The sol is freeze-dried.

(5) Calcination with a temperature ramp of 10°C.h^{-1} up to 380°C for 10 h in air produces a homogeneous spinel phase with all the Fe cations oxidized to Fe^{3+}. Therefore, further annealing in defined conditions of temperature and pO_2 is required to obtain a good ratio of oxygen to metal.

(6) Thermal treatment at 460°C is performed for 3 h under 1.4×10^{-24} Pa obtained from suitable $N_2/H_2/H_2O$ gas mixtures and air-cooled (23).

The second synthesis method consists of the following idealized mechanical reaction:

$$Fe_2O_3 + 1/2\ TiO_2 + 1/2\ Fe \rightarrow Fe_{2.5}Ti_{0.5}O_4. \quad [4]$$

The starting powders are anatase titanium dioxide (Degussa), ferric oxide (TCR), and iron (Prolabo). Continuous grinding was performed in a planetary ball mill (Fritsch Pulverisette 7) with two different values of the powder to ball weight ratio R, namely 1/40 and 1/20. The grinding tools are made of steel (Fe–13%Cr), the volume of the vial is approximately 45 cm^3, and seven balls of diameter $\varnothing \approx 13$ mm were used. The powders, in stoichiometric proportions, and balls were introduced in vials and sealed in a glove box under argon atmosphere. The powders were milled for times varying from 1 to 8 h. The specific shock power, P, released by the balls to the powders during the ball-milling process, which is the product of the shock frequency and the kinetic energy, was calculated for our experimental conditions from the model of Abdellaoui and Gaffet (41). P is about 2.7 and 1.3 W/g/ball for $R = 1/40$ and 1/20 respectively. Milling experiments were also conducted on oxide powder mixtures of α-Fe_2O_3 and TiO_2 to follow correctly the evolution of reactants during the mechanochemical treatment and also to test the miscibility of α-Fe_2O_3 and TiO_2 oxides. The powders were milled with a ball-to-powder ratio of 1/20 under air atmosphere. The influence of adding stearic acid on the final particle size was also studied in the latter case.

3.2. Techniques

The milled powders were chemically analyzed by ICP for two elements, carbon and chromium, in order to determine possible contamination by steel grinding tools.

The mean particle diameter of titanium ferrite powders is inferred from specific surface area measurements (AUTOSORB-1) and scanning electron micrographs (SEM)(JEOL JSM-6400F). The specific surface area was deduced from the BET equation using a least-squares refinement method.

The resulting powders were all characterized by X-ray diffraction (XRD) using a D5000 diffractometer with Cu$K\beta$ radiation and by ^{57}Fe Mössbauer spectrometry. The ^{57}Fe Mössbauer spectra are recorded with a constant acceleration spectrometer and a ^{57}CoRh source.

Data from XRD patterns were obtained with the DIFFRACT-AT program. XRD line profile analysis was performed to determine the average crystallite size and strain. The correction for the instrumental broadening is calculated from a standard reference material, annealed BaF_2 (42). The information deduced from the peak broadening depends on the line shape. Two main cases are considered. First, if the experimental line shape is Lorentzian, as in the case for ground powders (43), the peak broadening due to the sample is calculated from

$$\beta^* = \frac{1}{\varepsilon} + \frac{\eta}{d^*} \quad [5]$$

where β is the integral breadth, ε is the parameter linked to crystallite or domain size and shape, and η is the parameter related to strain. $\beta^* = \beta \cos\theta/\lambda$ and $d^* = 2 \sin\theta/\lambda$ are the reduced coordinates depending on the diffraction angle θ and the wavelength λ. The average crystallite size and strain are extracted from the so-called Williamson and Hall plot. Second, if the experimental line shape is Voigtian, as for

powders obtained by soft chemistry (44), the peak broadening is calculated from

$$\beta^{*2} = \frac{\beta^*}{\varepsilon} + \eta^2 \times d^{*2}. \quad [6]$$

The average crystallite size and strain are then extracted from a Halder and Wagner plot.

Particle shapes and structural defects of some powders were further characterized by high resolution transmission electron microscopy (HRTEM).

The coercivity of samples was measured with a M2100 50 Hz hysteresymeter.

3.3. Powder Reactivity under Gas Mixture

The oxidation and reduction reactions in various samples were studied by thermogravimetry (SETARAM TAG 24). The experimental procedure has already been published (23). The symmetric thermobalance is able to measure weight variations of about 0.001%.

4. RESULTS AND DISCUSSION

4.1. Study of Ground Mixtures of α-Fe_2O_3 and TiO_2

Table 1 gives carbon and chromium impurity contents in powders milled with steel grinding tools. The contamination level becomes significant after 8 h of grinding but it remains reasonable for the present study. In any case, it is much lower than contamination often reported (37, 38).

The average particle diameters of powders ground with or without stearic acid, deduced from surface specific measurements, are compared as a function of milling time in Table 2. They generally increase with milling time except when stearic acid is added to powders. In that case, powder particles tends to disaglomerate after a first step of aggregation, as stearic acid acts as a lubricant. Besides particle size, the average crystallite size deduced from XRD analysis decreases with milling time, while lattice strain increases. A slight decrease of lattice strain is observed when crystallite sizes are smaller than 15 nm. This could be due to an annihilation of defects at grain boundaries for grain sizes smaller than 15 nm. In conclusion, as-milled powders consist of polycrystals made from grains of about 10 nm.

TABLE 1
Carbon and Chromium Contamination Amounts, Estimated by ICP Analysis, as a Function of Milling Time for α-Fe_2O_3+TiO_2 Powders

Milling time (h)	C (ppm)	Cr (ppm)
0	—	< 100
1	440	385
2	504	200
6	485	350
8	753	605

TABLE 2
Specific Area Measurements and X-Ray Diffraction Analyses of α-Fe_2O_3+TiO_2

Milling time (h)	Specific area (m^2/g)	BET ∅ (nm)	DRX ∅ (nm)	Strain	Lattice constant a (Å)	Lattice constant c (Å)
	α-Fe_2O_3 + TiO_2, R = 1/20, under air temperature.					
0	42.2	—	—	—	—	—
1	10.7	112	99	0.018	5.035	13.741
2	9.5	127	68	0.024	5.033	13.738
6	8.1	148	51	0.031	5.038	13.772
8	6.1	196	15	0.020	5.040	13.797
	α-Fe_2O_3 + TiO_2, stearic acid, R = 1/20, under air atmosphere.					
0	42.2	—	—	—	—	—
1	11.4	100	297	0.018	5.030	13.731
2	12.4	92	133	0.021	5.036	13.761
6	16.7	68	29	0.016	5.037	13.775
8	18.2	62	28	0.015	5.034	13.757
	α-Fe_2O_3 + TiO_2 + Fe, R = 1/20, under argon atmosphere.					
0	10.3	—	—	—	—	—
1	9.0	133	49	0.017	5.039	13.751
2	8.0	150	57	0.023	5.045	13.739
4	7.4	163	35	0.025	5.046	13.768
6	4.4	271	44	0.030	5.055	13.777
8	4.6	261	5	0.015	5.059	13.809
	α-Fe_2O_3 + TiO_2 + Fe, R = 1/40, under argon atmosphere.					
0	10.3	—	—	—	—	—
1	6.3	182	—	0.035	5.049	13.800
4	4.1	279	12	0.021	8.465	—
6	3.8	306	8	0.009	8.457	—
8	4.0	290	8	0.013	8.462	—

Notes. The XRD line profile analysis is performed according to the Williamson and Hall method; the determination of lattice parameters is based on a least-squares refinement method.

The evolution of reactants and the intermixing of both oxides have been followed during milling of α-Fe_2O_3 and TiO_2 mixtures. The XRD patterns show that titanium dioxide disappears rapidly and that only the corundum phase remains during grinding. Such changes can be first ascribed to the amorphization of TiO_2 and second to the progressive formation of $[(3-x)/2](Fe_2O_3)x(TiO_2)$ solid solutions during the milling process. No mixture of pseudobrookite and corundum phases, although expected at low temperatures in the system Fe_2O_3–TiO_2, is detected. For large titanium contents, the stability range of the rhombohedral phase is increased at high temperatures (45); XRD results confirm once more that phases which are stable at high temperatures may also be obtained in metastable conditions by high-energy ball milling (46). In the case of pure TiO_2, for instance, milling allows the formation of high temperature–high pressure phase II TiO_2 from anatase titanium dioxide (47). The appearance of $[(3-x)/2](Fe_2O_3)x(TiO_2)$

solid solutions may also be suggested by the variation of the cell parameters of the rhombohedral phase as a function of milling time (Table 2). Indeed, the insertion of titanium in the corundum phase is accompanied by the replacement of 1 Fe^{3+} cation in octahedral coordination by 3/4 Ti^{4+} cations and 1/4 vacancies. Even if the Ti^{4+} ionic radius is smaller than that of Fe^{3+}, the very large oxygen–vacancy distance may explain the increase of lattice parameters.

The effect of a reducing thermal treatment of ball-milled α-Fe_2O_3 and TiO_2 powder mixtures was studied by thermogravimetry. Figure 1 presents the mass loss derivative curves as a function of temperature and milling time. As noticed in Fig. 1a, the curve of unmilled powders displays two features. The first corresponds to the transformation of haematite into magnetite. It is followed by the precipitation of metallic iron. For ground powders, the curves display several features. The first is attributed to the phase transformation: corundum structure (α-Fe_2O_3) to spinel structure with $\delta = 0$ (titanomagnetite $Fe_{3-x}Ti_xO_4$). The others, beginning at points (1), (2), (3), (4), and (5) in Fig. 1, are attributed to the precipitation of metallic iron, which can be dissociated in two steps for short grinding times due to the simultaneous insertion of titanium in the precipitate. Two

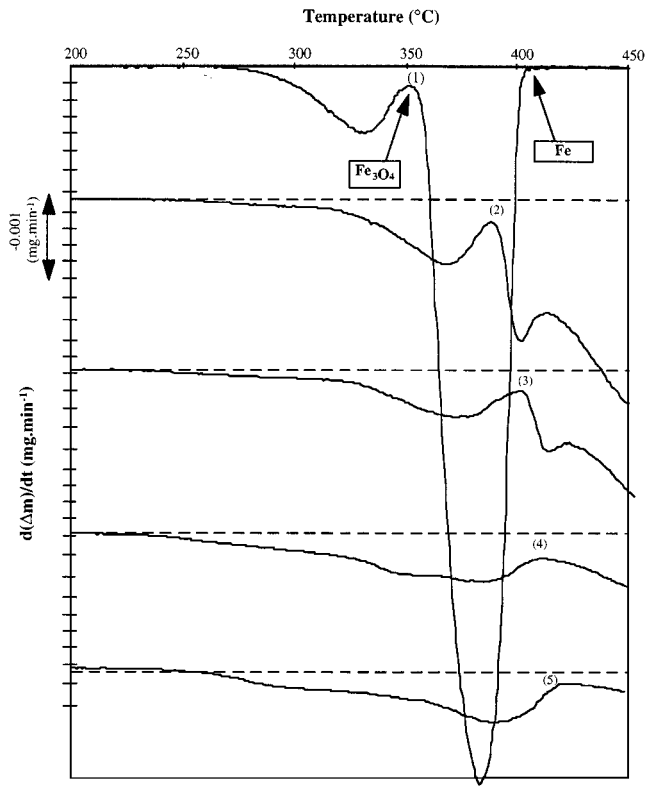

FIG. 1. DTG reduction curves $d\Delta m/dt = f(T)$ of α-$Fe_2O_3 + TiO_2$ milled 0, 1, 2, 6, 8 hours in stoichiometric amounts, under air atmosphere, with a powder-to-ball ratio of 1/20. H_2 flow is 0.16 l/min and temperature ramp 2°C/min.

phenomena, both related to the insertion of titanium in α-Fe_2O_3 during the milling process, can be observed for increasing milling times: a simultaneous increase of the beginning temperature of precipitation of the metallic phase and the mass loss at this temperature (Table 3). Before precipitation, the transformation of the corundum phase $(Fe^{3x}_{(18-6x)/(9+x)}Ti^{4+}_{6x/(9+x)}\square_{2x/(9+x)})O^{2-}_3$ to the spinel phase with $\delta = 0$ ($Fe^{2+}_{1+x}Fe^{3+}_{2-2x}Ti^{4+}_xO^{2-}_4$) is accompanied by the reduction of some Fe^{3+} cations to Fe^{2+}. The quantity of Fe^{3+} to be reduced increases with the Ti content in the rhombohedral phase. The mass loss increases, therefore, in the same way and allows x to be estimated. The Ti content x (Table 3) calculated from the mass loss recorded at points (1), (2), (3), (4), and (5) is again consistent with the formation of $[(3-x)/2](Fe_2O_3)x(TiO_2)$ solid solutions during the milling process. Moreover, the increase, with milling time, of the phase transformation temperature must also be attributed to the insertion of titanium into the solid solution since this cation is less mobile than iron cations. This is inferred from the iron–oxygen distance (Table 4), which is greater than the titanium–oxygen distance. Indeed, the mobility of a species is inversely proportional to the forces maintaining it in a defined position: since these forces, mainly originating from electrostatic interactions, decrease with the cation–oxygen distance, the mobility increases with ionic radius (1). Thermogravimetry, used here to demonstrate cation insertion during mechanical treatment, is seen to provide results which agree with the X-ray results.

The mechanical activation of α-$Fe_2O_3 + TiO_2$ powder mixtures followed by a reducing treatment allows titanium ferrite to be synthesized at low temperature (about 400°C) after only 6 h of mechanical activation. However, such thermal treatment induces grain growth, leading to particles of about 200 nm. The direct mechanosynthesis of titanium

TABLE 3

Temperature, Mass Loss, and Ti Content Corresponding to the Formation of the Spinel Structure during the Reducing Treatment of α-Fe_2O_3+TiO_2

Sample	Temperature (°C)	Mass loss (%)	Ti context x in $(Fe_{3-x}Ti_x)_{1-\delta}O_4$
(1)[a]	374 ± 1	− 2.9 ± 0.1	0.00
(2)[b]	384 ± 1	− 3.8 ± 0.1	0.21
(3)[c]	397 ± 1	− 3.9 ± 0.1	0.24
(4)[d]	406 ± 1	− 5.3 ± 0.1	0.53
(5)[e]	415 ± 1	− 5.4 ± 0.1	0.54

Notes. Temperature ramp 2°C/min; $dH_2 = 0.16$ l/min; all milling was realized with $R = 1/20$ under air atmosphere.

[a] starting materials.

[b] Ground 1 h.

[c] Ground 2 h.

[d] Ground 6 h.

[e] Ground 8 h.

TABLE 4
Cation–Oxygen Distances (and Their References) Used for Calculation of Lattice Parameters

Cation	Oxygen–cation length (Å)	Reference
$[Fe^{2+}]_A$	2.012	(54)
$[Fe^{2+}]_B$	2.132	(55)
$[Fe^{3+}]_A$	1.858	(54)
$[Fe^{3+}]_B$	2.020	(54)
$[Ti^{4+}]_B$	1.944	(53)

ferrite must thus be investigated to prepare ferrites with nanometer-sized grains.

4.2. The Formation of the $Fe_{2.5}Ti_{0.5}O_4$ Spinel Structure by Mechanosynthesis

As Fe_2O_3 is known to transform into Fe_3O_4 under reducing conditions, iron has been added to the previous oxide mixtures to mechanosynthesize the titanium ferrite directly.

The formation of the spinel phase is followed as a function of milling conditions by X-ray diffraction. With a powder-to-ball weight ratio R of 1/20 and after eight hours of milling, the diffraction peaks of α-Fe_2O_3 and Fe are always clearly observed but are broadened due to crystallite size reduction and accumulation of lattice strain. That means that the grinding conditions are not sufficiently energetic to induce a rapid-enough direct synthesis. With $R = 1/40$ (Fig. 2), the spinel phase appears after 1 h 30 min., and all the peaks on the XRD pattern are assigned to the spinel phase after four hours. This was confirmed by Mössbauer spectrometry (Fig. 3). As expected, Mössbauer spectra of the starting powders display the classical sextuplets associated with α-Fe_2O_3 and Fe. After grinding for one hour, the two sextuplets are always present but a dissymetric doublet corresponding to the spinel phase is observed. With the prolongation of milling time the hyperfine magnetic sextets disappear and are gradually replaced by the dissymetric and broadened doublet. The Mössbauer spectrum of powders milled for 4 h is identical to the spectrum for a powder milled for 8 h.

The coercive field has been measured as a function of milling time and R (Fig. 4). In the early stages of grinding, it increases, and then it slightly decreases. The first step can be attributed to the appearance of Fe^{2+} in the crystalline structure of Fe_2O_3 due to the reducing milling conditions, which are known to improve the magnetostrictive properties of the material and would explain the increase in coercive field (48). An assumption for the slight decrease of coercive field may be the reduction of crystallite size. Indeed, it is often reported that for grain sizes lower than a characteristic value, a superparamagnetic behavior appears, causing a decrease in the coercive field (49, 50).

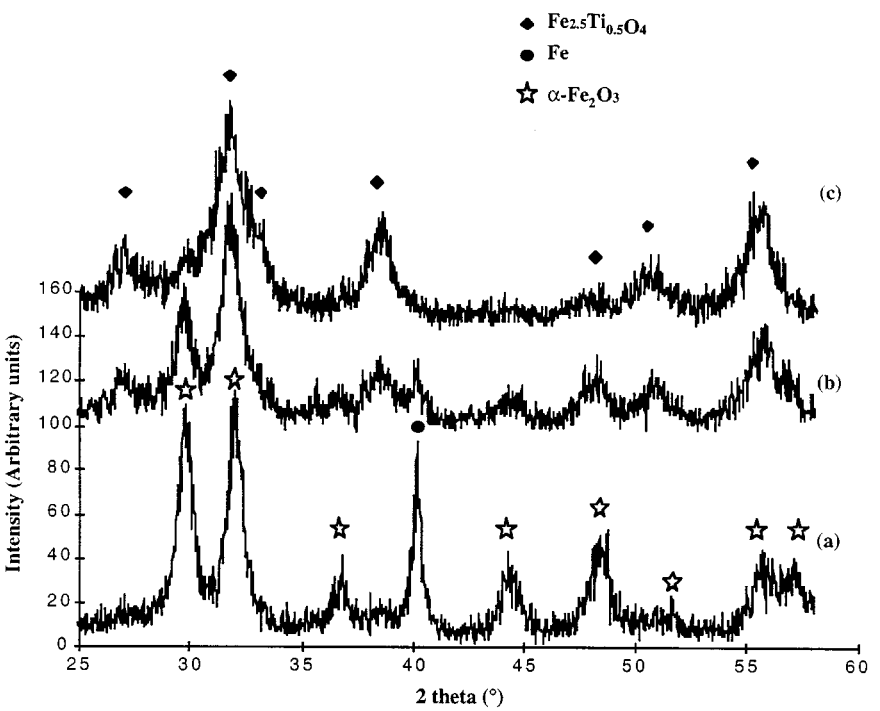

FIG. 2. X-ray diffractograms of α-Fe_2O_3 + TiO_2 + Fe ground (a) 1 h, (b) 1 h 30 min, and (c) 4 h in stoichiometric amounts, under argon atmosphere, with a powder-to-ball ratio of 1/40.

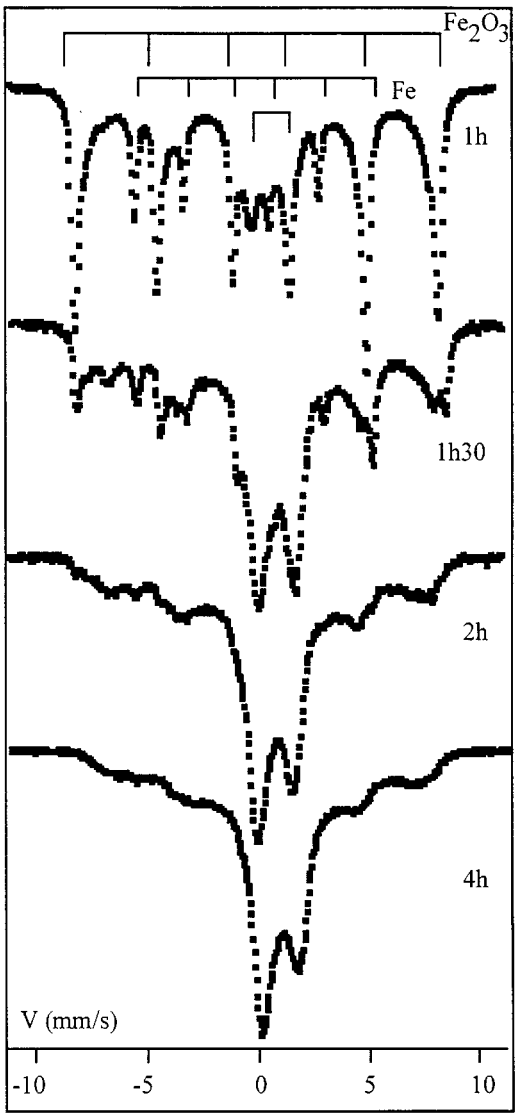

FIG. 3. ^{57}Fe room-temperature Mössbauer spectra of α-Fe_2O_3 + TiO_2 + Fe milled (a) 1 h, (b) 1 h 30 min, (c) 2 h, and (d) 4 h in stoichiometric amounts, under argon atmosphere, with a powder-to-ball ratio of 1/40.

In view of the results of previous sections, the general mechanism of titanium ferrite mechanosynthesis may be divided into at least two stages. The formation of solid solutions $[(3-x)/2](Fe_2O_3)x(TiO_2)$ (Fig. 1 and Table 2), which takes place by repeated fracture and welding of the constituent powder particles, is followed by the nucleation and gradual formation of the spinel phase (Figs. 2 and 3).

4.3. Comparison of the Mechanosynthesized Titanomagnetite with Those Prepared by Soft Chemistry

Powders prepared by soft chemistry are very well dispersed and homogeneous, with a grain size of about 18 nm, as shown in Fig. 5a. This value matches quite well the average

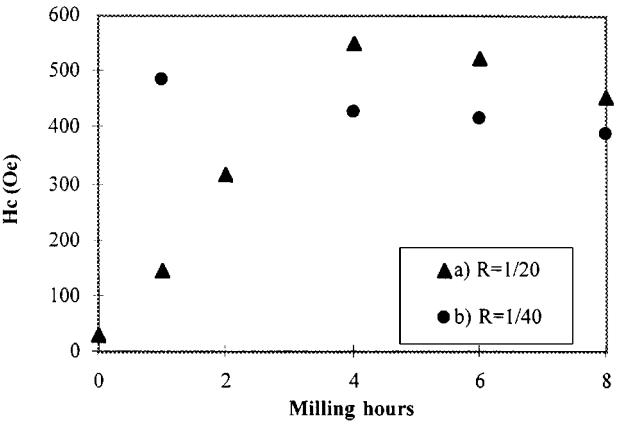

FIG 4. Coercivity of α-Fe_2O_3 + TiO_2 + Fe, milled under argon atmosphere in stoichiometric amounts, as a function of milling time with a powder-to-ball ratio of (a) 1/20 and (b) 1/40.

particle diameter deduced from specific area measurements ($S_{BET} = 68.5\ m^2 \cdot g^{-1}$, which yields a diameter of 18 nm) and the crystallite size deduced from XRD results, $\varnothing_{XRD} = 19.7$ nm. In contrast, ground powders consist of aggregates of nanometric crystallites. The average size of the aggregates is approximately 100–200 nm (Table 2) and the size of small crystallites in aggregates is about 15 nm (Fig. 5b and Table 2).

The oxidation behavior of both powders has been studied by thermogravitry (Fig. 6). The oxidation in the spinel phase leads to a weight gain of 4.1% for the powder obtained by soft chemistry (Fig. 6a) and 4.64% for the ball-milled powder (Fig. 6b). As the theoretical weight gain, 5.27%, is larger than these values, there is already significant oxidation of the Fe^{2+} cations at ambient temperature. These oxidations have been calculated: 22% for soft-chemistry powders ($\delta = 0.040$ in the formula $(Fe_{2.5}Ti_{0.5})_{1-\delta}O_4$); and 12% for ground powders ($\delta = 0.022$). This may be related to the agglomeration state of ground powders, which limits the oxidation process at ambient temperature. The difference in the agglomeration state between the two powders also explains that the DTG peaks are shifted toward high temperatures for ground powders. Indeed, the reactivity of a powder to oxidation is related to the gas/solid interface which, according to the above-mentioned specific area measurements, is considerably reduced during grinding. Therefore, despite smaller crystallite size, the reactivity of a ground powder is smaller than that of the sample obtained by the soft chemistry route. The DTG curve displays one single peak for the powder obtained by soft chemistry (Fig. 6a); it can be attributed to the oxidation of Fe^{2+} being located only in octahedral sites, as expected from the Néel model. In contrast, the two DTG peaks observed for mechanosynthesized powders (Fig. 6b) may be explained in terms of a cationic inversion induced by the milling process, which could cause the appearance of Fe^{2+} cations in A sites.

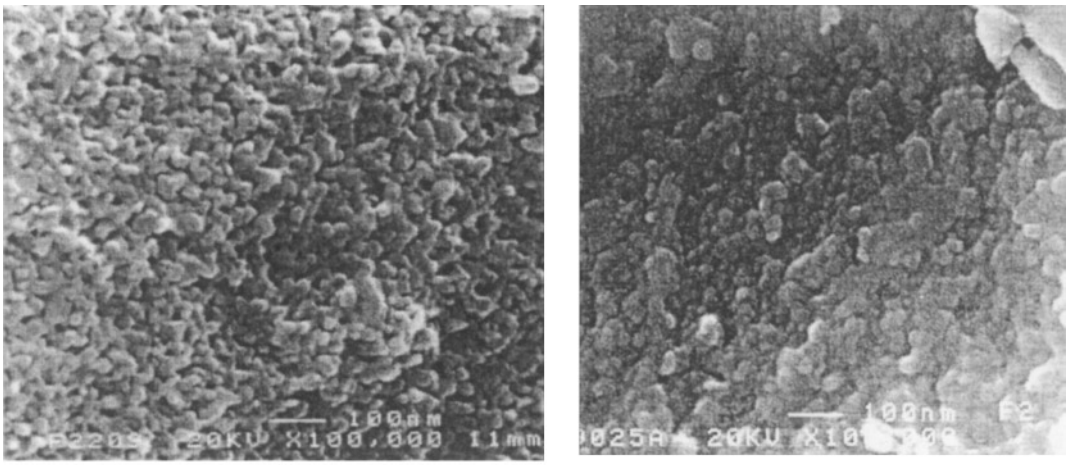

FIG. 5. S.E.M. micrographs of $Fe_{2.5}Ti_{0.5}O_4$ synthesized by (a) soft chemistry and (b) mechanosynthesis (4 h, $R = 1/40$, under argon).

Although the tetrahedral coordination is unfavorable according to crystal field theory (51), Fe^{2+} cations reside in the two sublattices in the case of ground powders. Again the effect of forced atomic jumps during ball milling on the structure results in an enhancement of the trend toward a random repartition between the two types of sites (52). Cation redistribution during the grinding process is in agreement with previous observations in Zn, Ni, and Mg ferrites (29). In the case of Ti ferrites obtained by mechanosynthesis, a rough quantitative analysis (1) from the area of the two DTG peaks allows calculation of the Fe^{2+} content for each site: $(40 \pm 10)\%$ in B sites and $(60 \pm 10)\%$ in A sites. Indeed, the temperature at which oxidation occurs is governed by the mobility of ions. As explained previously, there is a correlation between the mobility and the cation–oxygen bond length for both octahedral and tetrahedral sites of the spinel structure. B-site Fe^{2+} cations (O^{2-}–Fe^{2+} length = 2.132 Å) are more mobile than A-site Fe^{2+} cations (O^{2-}–Fe^{3+} length = 2.012 Å), so they are oxidized near 200°C, whereas the cations in

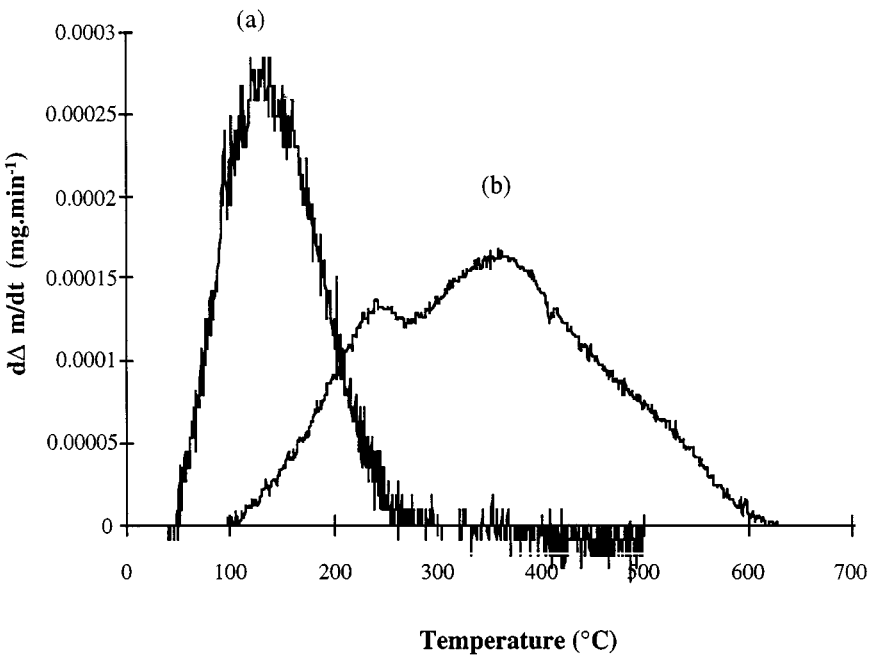

FIG. 6. DTG oxydation curves $d\Delta m/dt = f(T)$ of $Fe_{2.5}Ti_{0.5}O_4$ synthesized by (a) soft chemistry and (b) mechanosynthesis (4 h, $R = 1/40$, under argon).

A sites are oxidized only above 400°C (1). These oxidation temperatures must be compared only for phases with the same particle size and the same agglomeration state.

Figure 7 compares the XRD patterns of the spinel phases synthesized by soft chemistry and mechanosynthesis. The diffraction peaks are consistent with a single phase material. The diffraction peaks of the mechanosynthesized spinel phase are broadened due to crystallite sizes and lattice strains. Indeed, the lattice strain in the ball-milled spinel phase, $\eta = 0.021$, is higher than the comparable value for the spinel phase obtained by soft chemistry, $\eta = 0.000$. The lattice parameters of both materials are different, $a_0 =$ 0.8403 nm ($\pm$ 0.0001) for the spinel phase obtained by soft chemistry and $a_0 = 0.8465$ nm ($\pm$ 0.0001) for the ground product. This is to be compared with the mean value reported in the literature for titanium ferrites with large grains $a_0 \approx 0.844$ nm (15–19). These differences can be explained by two phenomena: the partial oxidation at ambient temperature and the presence of Fe^{2+} cations in A sites. The cation–oxygen distances used for the calculation of the lattice parameter by the Poix method (53–55) are given in Table 4, while experimental, calculated, and published lattice parameters are compared in Table 5. The calculated values are in good agreement with the experimental ones. The increased lattice parameter measured for mechanosynthesized powders can be explained by the redistribution of Fe^{2+} cations on tetrahedral sites during milling. It is consistent with Fe^{2+} cations located in both B sites (45%) and A sites (55%). This distribution is in good agreement with the oxidation DTG analyses. The decreased lattice parameter for powders synthesized by soft chemistry results from a partial oxidation of the isolated nanometric crystallites at ambient temperature.

HRTEM micrographs (Fig. 8) demonstrate that there are no structural defects in powders synthesized by soft chemistry (Fig. 8a), a finding that is in agreement with XRD results. The crystallites exhibit an hexagonal shape. This particular shape is already observed in the precipitated powders. A surrounding boundary of an amorphous nature is formed on some particles after the reducing treatment. This is consistent with the aforementioned partial oxidation in room conditions, which should take place near the particle surfaces. Several defects—stacking defects and lattice distortions—are observed in ball-milled powders in accordance with XRD results (Fig. 8b). The crystallite size determined by HRTEM (about 10 nm) is the same as the size derived from XRD analyses (12 nm).

TABLE 5

Experimental and Calculated (Poix Method) Lattice Parameters as a Function of Fe^{2+} Amounts in A Sites and as a Function of the Deviation from Stoichiometry δ

δ	$[Fe^{2+}]_A$ amount			
	0	0.5	0.7	1
0	$a = 8.420$ Å theoretical $a = 8.425$ Å exp. (16, 17)	$a = 8.460$ Å theoretical $a = 8.465$ Å exp. (15)		$a = 8.495$ Å theoretical
0.022	$a = 8.410$ Å theoretical		$a = 8.465$ Å exp. mechanosynthesis	$a = 8.485$ Å thoretical
0.040	$a = 8.400$ Å theoretical $a = 8.403$ Å exp. soft chemistry			
0.158	$a = 8.337$ Å exp. soft chemistry			

Note. Parentheses indicate references from the literature.

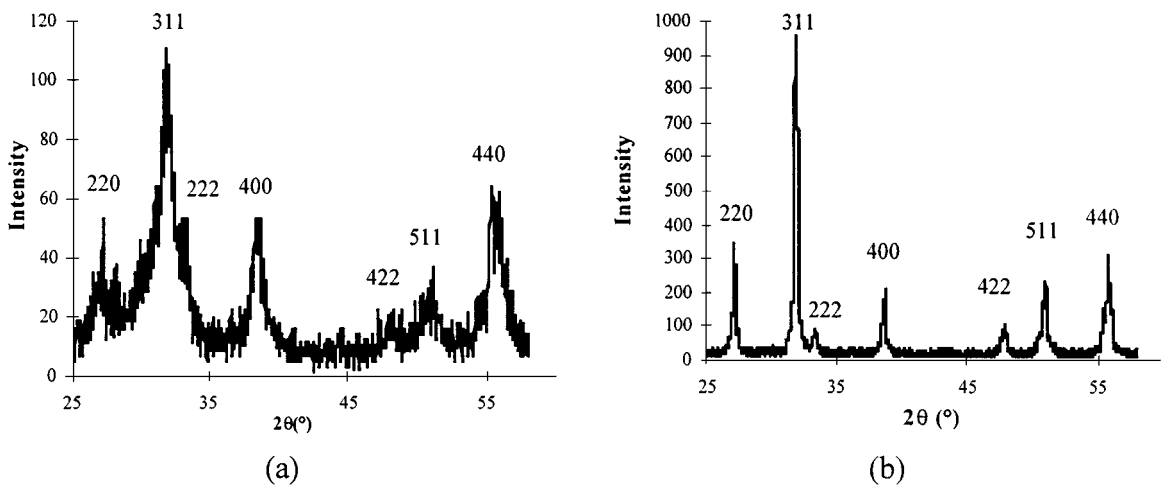

FIG. 7. X-ray diffractograms of $Fe_{2.5}Ti_{0.5}O_4$ synthesized by (a) soft chemistry (b) mechanosynthesis (4 h, $R = 1/40$, under argon).

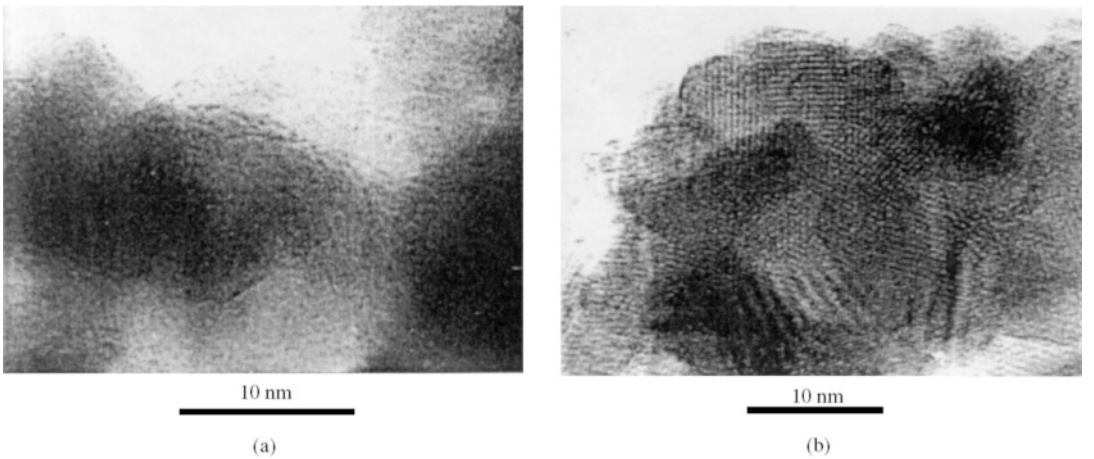

FIG. 8. H.R.T.E.M. micrographs of $Fe_{2.5}Ti_{0.5}O_4$ synthesized by (a) soft chemistry and (b) mechanosynthesis (4 h, $R = 1/40$, under argon).

Mössbauer spectra of the titanomagnetites synthesized by mechanical alloying and by soft chemistry are shown in Fig. 9. The two series of spectra are very different and very complex. An interpretation of all details of the spectra is out of reach. As emphasized by Russo *et al.* (56) for natural spinels, the simultaneous presence of iron in different oxidation states and coordination geometries and the existence of a variety of more remote cation neighbors of a given Fe atom give rise to an a priori unknown number of (generally overlapping) peaks. Besides heterogeneities in chemical composition, which are discussed below, size effects are a source of further complexity of spectra, as is the case with the asymmetry observed (Fig. 9a). Information can nevertheless be extracted from some undisputed features of the observed spectra, namely the sextets with the largest hyperfine fields, S1 and S2, whose peaks on the negative velocity side are indicated in Fig. 9a by A1 and A2. The spectrum of the spinel phase synthesized by soft chemistry (Fig. 9a) corresponds to the Mössbauer spectrum expected for a ferrimagnetic polycrystalline material with the superposition of more than two magnetic hyperfine sextets (57, 58). Clear differences exist, however, from the spectrum published by Melzer *et al.* for a titanoferrite of the same composition (58). In particular, the hyperfine field of the outer sextet is much larger in our case, H1 = 486 kG, than for the titanomagnetite investigated by Melzer *et al.*, $Fe_{2.5}Ti_{0.5}O_4$, H1 = 447 kG (58). The field value determined by Melzer *et al.* is consistent with the results of Tanaka and Kono for $Fe_{3-x}Ti_xO_4$ ($0 \leq x \leq 0.33$) (57), showing that the hyperfine field described in the latter work decreases with Ti content (Fig. 10). A reasonable range of values for the hyperfine field H1 for $x = 0.50$ is 431(Q)–452(L) kG, calculated from a linear (L) and a quadratic (Q) extrapolation of the published values. We must conclude that the outer sextet S1 that we observe here cannot be associated with a titanomagnetite whose Ti content is $x = 0.50$. The x dependence of the hyperfine field (Fig. 10) is indeed mainly associated with a titanoferrite whose Ti content is less than at most $x = 0.10$. We have neglected a classical but small decrease of the measured field related to particle size (59) (of the order of 3 kG) to derive the latter Ti content. An eventual change of the hyperfine field of surface atoms has also been neglected: for α- and γ-Fe_2O_3, the hyperfine field of surface atoms is smaller than the field of Fe atoms in the bulk (by about 4% for α-Fe_2O_3) (50). In both cases, the upper Ti content is overestimated, so that heterogeneities of the Ti content exist in the analyzed powder. The aforementioned Mössbauer characteristics are therefore accounted for by chemical composition variations inside each particle. Fe–Ti segregation may be attributed to an immiscibility gap in the spinel system below 500°C, as mentioned for Ti ferrites with high substitution content (19). However, the particles are found to be homogeneous by *in situ* X-ray investigations during the reducing annealing. The heterogeneities are, then, related rather to kinetics effects linked to partial oxidation of the iron cations occurring when nanoparticles are studied in room conditions. Oxidation is controlled by transport within the grains. Vacancies, which are created at the surface during the incorporation of oxygen in the lattice, diffuse in the particle. The vacancy diffusion occurs in conjunction with the counterdiffusion of the more mobile cations, here the iron cations (2). Therefore, whereas near the surface there are mainly iron Fe^{3+} cations, in the bulk of the particle the Fe^{2+} and titanium cations are predominant. The measured field H1 is indeed consistent with a Fe_2O_3 surface layer. The subspectrum S2 with broad lines has an average field H2 of 455 kG. It results then from the superposition of various contributions, including Fe^{3+} in A sites of a Ti-rich titanomagnetite and $Fe^{\approx 2.5+}$ in B sites (arising from electron hopping between Fe^{3+} and Fe^{2+} pairs). Even

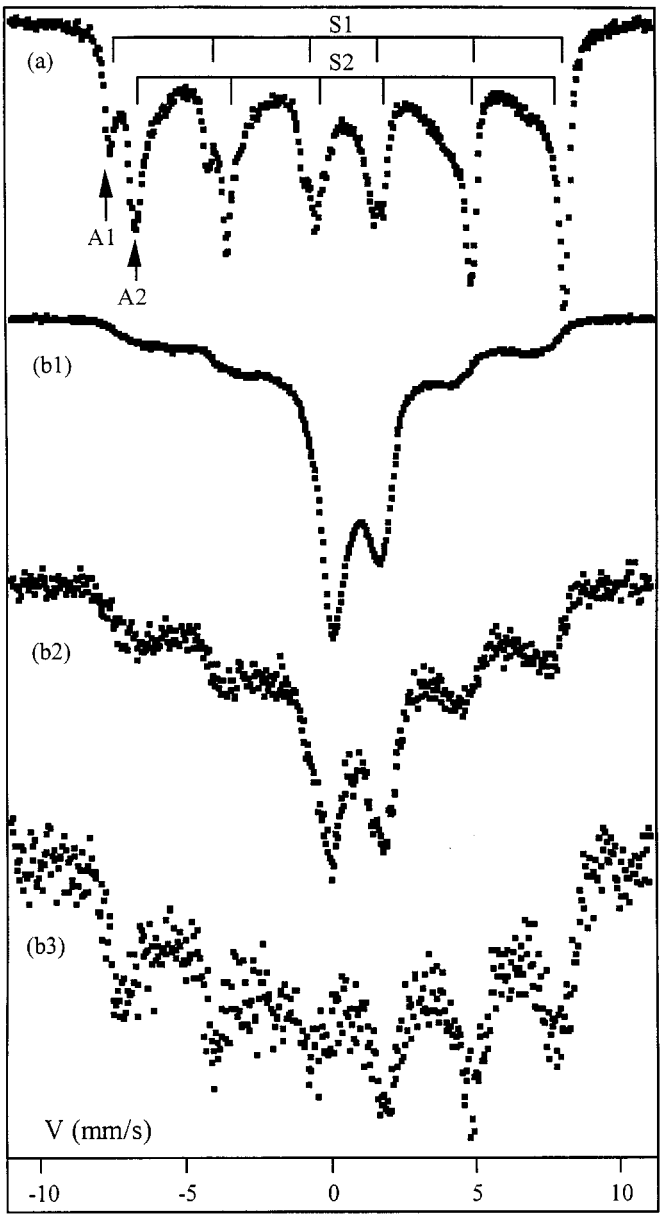

FIG. 9. (a) ^{57}Fe Mösssbauer spectra of $Fe_{2.5}Ti_{0.5}O_4$ synthesized by soft chemistry (room-temperature spectra). It displays several sextets; the outer subspectrum S1, whose field is easily calculated, is related to Fe^{3+} at A sites with a typical hyperfine field H1 of 486 $\pm$ 2 kG. The subspectrum S2 has an average field H2 of 455 $\pm$ 2 kG. A noticeable characteristic is the asymmetry of the groups of lines A1 and A2. The first absorption minimum A1 on the negative velocity side around -8 mm/s looks indeed much smaller than the next minimum A2 around -7 mm/s. (b) ^{57}Fe Mössbauer spectra of $Fe_{2.5}Ti_{0.5}O_4$ synthesized by high-energy ball milling (4 h, $R = 1/40$, under argon): (b1) room temperature spectra; (b2) 200 K spectra; (b3) 100 K spectra.

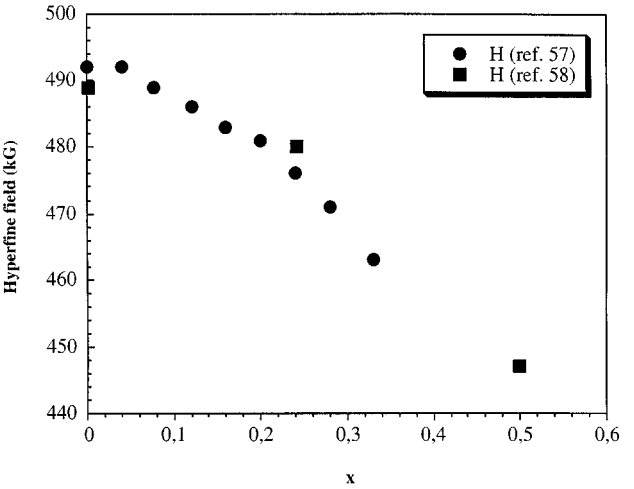

FIG. 10. Room-temperature hyperfine field of the outer sextuplet S1 of Mössbauer spectra of titanomagnetite as a function of Ti content.

if other Fe ions' environments with a distribution of iron and titanium neighboring atoms also contribute to the observed spectrum, the spectrum is mainly in agreement with particles with a Ti-rich core and a Fe-rich shell.

The Mössbauer spectra of the mechanosynthesized titanomagnetite (Fig. 9b) are similarly not simple to analyze. The shape of the room-temperature spectrum (Fig. 9b1), with a broad, featureless set of four external lines, a characteristic field of about 420 kG, and an intense asymmetric central doublet, suggests that superparamagnetic relaxation takes place in the sample (50, 60, 61). The room-temperature spectrum thus cannot be associated with classical magnetic behavior, as it is quite different from the spectrum expected for coarse-grained $Fe_{2.5}Ti_{0.5}O_4$ or more generally for coarse-grained $Fe_{3-x}Ti_xO_4$ for $0 \leq x \leq 0.5$ (57, 58). For $0.5 \leq x \leq 1$, the Néel temperature decreases to about 120 K (62). The corresponding room-temperature spectra have shapes (57, 58, 62) which differ from the one we observe. The assumption of superparamagnetic relaxation, which is consistent with an average crystallite size of 15 nm, is confirmed by spectra recorded at 200 and 100 K (Fig. 9b2, 9b3). They show a progressive increase of the magnetically split part of the spectra when the temperature decreases. This increase is related to a distribution of grain sizes, classically broad in ground powders, which results in a distribution of blocking temperatures: the bigger a grain, the higher its blocking temperature (50). At 100 K, the spectrum consists of a broad magnetic background and a set of narrower lines. The hyperfine field associated with the two intense outer lines is 465 $\pm$ 5 kG at 100 K, a value quite consistent with a Fe^{3+} field at low temperature. A field of about 450 kG is indeed calculated from the Mössbauer spectrum at 90 K of $Fe_{2.3}Ti_{0.7}O_4$ (50). The distribution of crystallite sizes in titanoferrites prepared by soft chemistry has a slightly larger mean but is narrower than the size distribution in mechanosynthesized ferrites. This explains why superparamagnetic behavior, which originates from the smallest crystallites, is

clearly observed only in the latter case. The room-temperature spectra (Figs. 9a and 9b1) finally show that the hyperfine fields associated with the biggest particles of the mechanosynthesized ferrite are smaller than the field of site S1 of the soft-chemistry ferrite. This is consistent with the oxidation behavior of the two powders described above, which results in much narrower fluctuations of composition in the grains of the mechanosynthesized ferrite than in those of the soft-chemistry ferrite.

The coercive field of titanomagnetite obtained by mechanosynthesis is about 430 Oe. This high value is due to the bigger particles of ground powders creating a large size distribution, as expected from Mössbauer results. This field is approximately twice that of titanomagnetite obtained by soft chemistry (270 Oe). Such differences may be partly attributed to the difference of stoichiometry in oxygen between the powders. There are more Fe^{2+} cations in the ground spinel phase than in powder synthesized by soft chemistry and some of them, as seen previously, are located on tetrahedral sublattices. Due to the magnetostrictive properties of Fe^{2+} cations, in particular in A sites, the coercive field of the mechanosynthesis powder is therefore higher than the fields of powders obtained by the chemical route. The aforementioned lattice strains in ground powders should also increase the anisotropy and thus the coercivity.

5. CONCLUSIONS

Nanocrystalline $Fe_{2.5}Ti_{0.5}O_4$ titanomagnetites have been synthesized by direct milling of powder mixtures of $Fe + \alpha$-$Fe_2O_3 + TiO_2$ in stoichiometric proportions. The spinel phase is obtained after 4 h of grinding at room temperature without significant contamination. Mechanical activation of α-$Fe_2O_3 + TiO_2$ powder mixtures followed by reducing treatments at low temperature ($\leq 400°C$) also allows the spinel phase to be synthesized, but with grain sizes around 200 nm. The $Fe_{2.5}Ti_{0.5}O_4$ spinel phases obtained by direct mechanosynthesis and by soft chemistry have been compared. Mechanosynthesis leads to aggregates of nanocrystallites (≈ 15 nm) of ferrite and thus preserves $\delta \approx 0$ in room conditions, whereas soft chemistry leads to grains of about 18 nm. In the latter powders, grains are separated from each other. Oxidation phenomena thus occur at the surface of grains in the soft chemistry powders and lead to materials with a higher δ. Mössbauer spectra agree with the previous conclusions on the differences in oxidation behavior and in crystallite size distribution. They demonstrate that heterogeneities of the titanium content exist in soft chemistry powders, while superparamagnetic behavior is demonstrated in the mechanosynthesized ferrites. The study of the oxidation behavior demonstrates further that in powders synthesized by soft chemistry, Fe^{2+} are located in octahedral sites, while in mechanosynthesized powders, Fe^{2+} occupy both sites. A rough quantitative analysis from both X-ray diffraction and thermogravimetric experiments gives $40 \pm 10\%$ of Fe^{2+} in B sites and $60 \pm 10\%$ in A sites.

ACKNOWLEDGMENTS

The authors would like to thank Dr. C. M. Valot and Dr. F. Bernard for their guidance during X-ray analysis; B. Berini, S. Collin, P. Delcroix, Dr. Y. Champion, Dr. D. Aymes, and Prof. B. Malaman for their help in the experiments; and Dr. M. Guyot, Dr. B. Gillot, and Prof. J.C. Niepce for helpful discussions.

REFERENCES

1. B. Gillot, *J. Solid State Chem.* **113,** 163 (1994).
2. P. Perriat, B. Domenichini, and B. Gillot, *J. Phys. Chem. Solids* **57,** 1641 (1996).
3. M. S. Multani and P. Ayyub, *Condens. Matter News* **1,** 25 (1991).
4. R. Dieckmann, *Ber. Bunsen-Ges. Phys. Chem.* **86,** 112 (1982).
5. W. O'Reilly, *J. Magn. Magn. Mater.* **137,** 167 (1994).
6. P. W. Readman and W. O'Reilly, *J. Geomag. Geoelectr.* **24,** 69 (1972).
7. M. Ozima and M. Ozima, *Phys. Earth Planet. Interiors* **5,** 87 (1972).
8. C. M. Keefer and P. N. Shive, *J. Geophys. Res.* **86,** 987 (1981).
9. Y. Hamano, *J. Geomag. Geoelectr.* **41,** 65 (1989).
10. T. Nishitani and M. Kono, *J. Geomag. Geoelectr.* **41,** 19 (1989).
11. V. Kropacek and M. Lastovickova, *J. Geophys.* **48,** 40 (1980).
12. B. Gillot and F. Jemmali, *React. Solids* **2,** 95 (1986).
13. B. Gillot and F. Jemmali, *Mater. Chem. Phys.* **15,** 577 (1986).
14. E. J. Verwey and E. L. Heilman, *J. Chem. Phys.* **15,** 174 (1947).
15. S. Akimoto, *J. Geomagn. Geoelec.* **61,** 1 (1954).
16. L. Néel, *Adv. Phys.* **4,** 191 (1955).
17. R. Chevalier, J. Bolfa, and S. Mathiew, *Bull. Soc. Franc. Min. Crist.* **78,** 307 (1955).
18. W. O'Reilly and S. K. Banerjee, *Phys. Lett.* **17,** 237 (1965).
19. A. Trestman-Matts, S. E. Dorris, S. Kumarakrishnan, and T. O. Mason, *J. Am. Ceram. Soc.* **66,** 829 (1983).
20. H. S. C. OíNeill and A. Navrotsky, *Am. Mineral.* **68,** 181 (1983).
21. J. P. Jolivet, "De la solution å l'oxyde." InterEditions/CNRS Editions, Paris, 1994.
22. A. Rousset, F. Chassagneux, and J. Paris, *J. Mater. Sci.* **21,** 3111 (1986).
23. D. Aymes, N. Millot, V. Nivoix, P. Perriat, and B. Gillot, *Solid State Ionics* **101–103,** 261 (1997).
24. C. C. Koch, *Annu. Rev. Mater. Sci.* **19,** 121 (1989).
25. V. V. Boldyrev, N. Z. Lyakhov, Pavlyukhin, E. V. Boldyreva, E. Y. Ivanov, and E. G. Avvakumov, *Sov. Sci. Rev. B. Chem.* **14,** 105 (1990).
26. J. J. De Barbadillo, *Key Eng. Mater.* **77–78,** 187 (1993).
27. V. Sepelak, K. Tkacova, V. V. Boldyrev, and U. Steinike, *Mater. Sci. Forum.* **228–231,** 783 (1996).
28. V. Sepelak, M. Zatroch, K. Tkacova, P. Petrovic, S. Wissmann, and K. D. Becker, *Mater. Sci. Eng. A*, to appear.
29. K. Tkacova, V. Sepelak, N. Stevulova, and V. V. Boldyrev, *J. Solid State Chem.* **123,** 100 (1996).
30. G. Nicoara, D. Fratiloiu, M. Nogues, J. L. Dormann, and F. Vasiliu, *Mater. Sci. Forum* **235–238,** 145 (1997).
31. V. Sepelak, A. Yu. Rogachev, U. Steinicke, D. Chr. Uecker, F. Krummeich, S. Wissmann, and K. D. Becker, *Mater. Sci. Forum* **235–238,** 139 (1997).
32. G. Concas, F. Congiu, A. Corrias, C. Muntoni, G. Paschina, and D. Zedda, *Z. Naturforsch. A* **51,** 915 (1996).
33. C. Jovalekic, M. Zdujic, A. Radakovic, and M. Mitric, *Mater. Lett.* **24,** 365 (1995).
34. W. A. Kaczmarek and M. Giersig, *J. Phys. IV* (*France*) **7,** Colloque C1 (1997).
35. P. Matteazzi and G. Le Caër, *Mater. Sci. Eng.* **149,** 351 (1994).

36. S. J. Campbell, W. A. Kaczmarek, and G-M. Wang, *Nanostruct. Mater.* **6,** 735 (1995).
37. S. Linderoth, J. Z. Jiang, and S. Morup, *Mater. Sci. Forum* **235–238,** 205 (1997).
38. T. Kosmac and T. H. Courtney, *J. Mater. Res.* **7,** 1519 (1992).
39. W. A. Kaczmarek and B. W. Ninham, *IEEE Trans. Magn.* **30,** 732 (1994).
40. V. A. Sadykov, L. A. Isupova, S. V. Tsybulya, S. V. Cherepanova, G. S. Litvak, E. B. Burgina, G. N. Kustova, V. N. Kolomiichuk, V. P. Ivanov, E. A. Paukshtis, A. V. Golovin, and E. G. Avvakumov, *J. Solid State Chem.* **123,** 191 (1996).
41. M. Abdellaoui and E. Gaffet, *Acta Metall. Mater.* **43,** 1087 (1995).
42. J. I. Langford, Special Publication 846, p. 145. National Institute of Standards and Technology, 1992.
43. G. K. Williamson and W. H. Hall, *Acta Metall. Mater.* **1,** 22 (1953).
44. N. C. Halder and C. N. J. Wagner, *Adv. X-ray Anal.* **9,** 91 (1966).
45. R. W. Taylor, *J. Am. Ceram. Soc.* **46,** 278 (1963).
46. S. Begin-Colin, G. Le Caër, M. Zandona, E. Bouzy, and B. Malaman, *J. Alloys Comp.* **227,** 157 (1995).
47. S. Begin-Colin, G. Le Caër, A Mocellin, and M. Zandona, *Philos Mag. Lett.* **69,** 1 (1994).
48. M. P. Sharrock, *IEEE Trans. Magn.* **25,** 4374 (1989).
49. F. E. Luborski and T. O. Paine, *J. Appl. Phys.* **31,** 68 (1960).
50. J. L. Dormann, D. Fiorani, and E. Tronc, *Adv. Chem. Phys.* **98,** 283 (1997).
51. D. S. Mac Clure, *J. Phys. Chem. Solids* **3,** 311 (1957).
52. G. Martin and P. Bellon, in "Driven Alloys" (H. Ehrenreich and F. Spaepen, Eds.), Solid state Physics, Vol. 50, p. 189. Academic Press, New York, 1997.
53. P. Poix, "Liaisons interatomiques et propriétés physiques des composés minéraux, Suchet," Paris, 1966.
54. P. Poix, F. Basile, and C. Djega-Mariadassou, *Ann. Chim.* **3,** 159 (1975).
55. M. El Guendouzi, K. Sbai, P. Perriat, and B. Gillot, *Mater. Chem. Phys.* **25,** 429 (1990).
56. U. Russo, S. Carbonin, and A. Della Giusta, "Mössbauer spectroscopy applied to magnetism and materials science," Vol. 2, p. 207. Plenum, New York, 1996.
57. H. Tanaka and M. Kono, *J. Geomagn. Geoelect.* **39,** 463 (1987).
58. K. Melzer, Z. Simsa, M. Lukaslak, and J. Suwalski, *Cryst. Res. Technol.* **22,** 132 (1987).
59. S. Morup, J. A. Dumesic, and H. Topsoe, "Applications of Mössbauer Spectroscopy", (R. L. Cohen, Ed.), Vol. 2, Academic Press, New York, 1980.
60. V. U. Patil and R. G. Kulkarni, *Solid State Commun.* **31,** 551 (1979).
61. E. Tronc and J. P. Jolivet, *Mater. Sci. Forum* **235–238,** 659 (1997).
62. R. Vanleerberghe and R. E. Vandenberghe, *Hyperfine Interact.* **23,** 75 (1995).